Eur. Phys. J. Plus (2019) **134**: 189
DOI 10.1140/epjp/i2019-12508-3

THE EUROPEAN PHYSICAL JOURNAL PLUS

Regular Article

Features of the flow over a rotating circular cylinder at different spin ratios and Reynolds numbers: Experimental and numerical study

Mohammad Javad Ezadi Yazdi[1,a], Ali Safavi Rad[2], and Abdulamir Bak Khoshnevis[3,b]

[1] Department of Mechanical Engineering, Semnan University, Semnan, Iran
[2] Department of Mechanical Engineering, Islamic Azad University South Tehran Branch, Tehran, Iran
[3] Department of Mechanical Engineering, Hakim Sabzevari University, Sabzevar, Iran

Received: 25 October 2018 / Revised: 4 January 2019
Published online: 6 May 2019

Abstract. In this study, the characteristics of the flow in a rotating circular cylinder are investigated experimentally and numerically. The hot-wire anemometry is used to measure the mean velocity and turbulent intensity of the flow, also the k-ω SST model is used to extract the numerical results. The diameter of the cylinder is considered to be 20 mm. The effect of Reynolds number (Re) in the range of ($5900 \leq \mathrm{Re} \leq 11800$) and the spin ratio ($\alpha$) in the range of ($0 \leq \alpha \leq 0.525$) on the characteristics of the flow wake such as time-averaged velocity, turbulence intensity, higher-order central moments of the hot-wire velocity signals (*i.e.* skewness factor), Strouhal number, drag coefficient and flow pattern have been investigated. According to the experimental results, the cylinder rotation has led to change in the mean and fluctuation velocity profiles and the velocity reduction region has become smaller by increasing the Reynolds number. Furthermore, the symmetry of the flow is broken as the rotation ratio increases. Also, by increasing the rotation ratio, the positions of the stagnation and separation points are changed. It is found that with increasing the rotation ratio, the drag coefficient and the velocity reduction parameters are decreased.

1 Introduction

Recently, many researchers have intended to study the incompressible flow around a rotating circular cylinder using theoretical, experimental and numerical methods. Many applications of this field can be found in aerodynamic problems as well as engineering structures. The boundary layer flows can be controlled through using rotational cylinders or other control methods such as blowing, suction, surface roughness, and so on, which are mentioned in many papers, including Bearman [1], Radi *et al.* [2], Hak and Bushnell [3], Martin *et al.* [4], Griffin and Hall [5], Rao *et al.* [6] and Meena and Mittal [7]. According to Tokumaru and Dimotakis [8], the inclusion of forced rotary oscillations in cylinder's steady rotation can be helpful in increasing the lift coefficient as well as producing a substantial decline in the cylinder drag. For a rotating cylinder, constant spin rate in a viscous and uniform flow will change the flow field and vortex shedding which significantly modified the wake and caused a flow-induced vibration and the lift force. Modi *et al.* [9] indicated that flow past airfoils can be controlled by placing a rotating cylinder at proper location in the flow; such configuration could dramatically enhance the lift. Separation phenomenon is one of the major properties of such flows.

Many papers have focused on the stability phenomenon and the displacement of rotating circular cylinders. The first research effort was mainly to investigate the well-known Magnus's effect. Many of the examined cases showed a periodic flow field associated with the vortex shedding activity. In more detailed studies, the strong dependency between the flow instability and the critical value of $\alpha = U_\theta/U_\infty$ were reported, in which the effect of Reynolds number could be considered negligible; U_θ and U_∞ represent the peripheral velocity of the cylinder and the free flow velocity, respectively. A preliminary experimental study was carried out by Prandtl [10] on a rotating circular cylinder.

[a] e-mail: M.J.EzadiYazdi@semnan.ac.ir
[b] e-mail: khoshnevis@hsu.ac.ir

According to the results of his study, in low rotational speeds, the flow separation was occurred at the bottom of the cylinder. Also he declared that the maximum generated lift force by a rotating circular cylinder located in uniform flow field could not exceed 4π. However, the results of Tokumaru and Dimotakis [8] study was in contrast with this observation; they showed that the maximum lift force can exceed 4π. In a case study in $\mathrm{Re} = 3.8 \times 10^3$ and $\alpha = 10$, the calculated lift coefficient was 20% larger than 4π.

Studying the flows around the rotating cylinder in low Reynolds numbers has attracted many researchers. In a numerical study by Ingham and Tang [11], the governing Navier-Stokes equations were solved using a finite difference approach and the asymmetric flow in uniform viscous fluid within the Reynolds numbers in the range of 5 and 20, and the dimensionless ratio in the interval of 0 to 0.5 was investigated. In another study by Badr *et al.* [12] in low Reynolds numbers, the steady and unsteady flows were investigated numerically. They proposed the use of series expansion method to prevent the problems encountered in satisfying the boundary conditions in far downstream regions of the cylinder. The Reynolds numbers were in the range of 5 and 20 ($5 \leq \mathrm{Re} \leq 20$) and the dimensionless ratio was in $0 \leq \alpha \leq 3$.

Furthermore, Ingham and Tang [11] conducted numerical simulations for the steady and two-dimensional flow to develop the previous research for Reynolds numbers in the range of 60 and 100 and $0 \leq \alpha \leq 1$. Another work in the Reynolds number of 200 was done by Chen *et al.* [13], in which, an explicit pseudo-spectral approach was used for solving the governing equations. They found that when $\alpha = 3.25$, more than one vortex had shed in the flow downstream.

The studies of Kang [14] also played a significant role in this field. He used sequential numerical simulations in Reynolds numbers of $\mathrm{Re} = 40, 60, 100, 160$ and in the dimensionless ratio of $0 \leq \alpha \leq 2$. According to the obtained results, the flow instability changes logarithmically with respect to the increase of Reynolds number at $60 \leq \mathrm{Re} \leq 160$ and the maximum rotational ratio.

In another study, following the work of Chen and Patel [15], Mittal and Kumar [16] performed numerical simulations for the dimensionless ratio of $0 \leq \alpha \leq 5$ and Reynolds number of $\mathrm{Re} = 200$ and solved the incompressible Navier-Stokes equations by the use of finite-element approach. In addition, they analyzed the flow stability using a new method, which had led to many important theoretical results. They also obtained the unique solutions for the mentioned spin ratio. However, their most important result was to determine a new range for α, in which the flow becomes unstable. For $\alpha < 1.91$, the flow was time-dependent (non-stationary), by increasing α up to 4.37, the flow became steady; however, by further increasing of α at $4.34 < \alpha < 4.70$, the flow became unsteady again. In some other investigations, various characteristics of the laminar flow around a rotating cylinder have been investigated. Kang [14] studied the two-dimensional laminar flow around a rotating cylinder in a uniform shear flow and conducted numerical simulations at $\mathrm{Re} = 200$ and $\alpha = 5.5$.

Solving the flow around the cylinder in the medium Reynolds numbers ($\mathrm{Re} > 1000$) is much more difficult due to three-dimensional nature and dominancy of the turbulence effects. Badr *et al.* [17] investigated the effect of cylinder rotational speed in an unsteady flow in $10^3 \leq \mathrm{Re} \leq 10^4$ and $0.5 \leq \alpha \leq 3$, numerically and experimentally. Their results had an acceptable consistency, except for $\alpha = 3$. In another numerical work, Chew *et al.* [18] used a hybrid vortex method in $\mathrm{Re} = 1000$ and $0.5 \leq \alpha \leq 6$. They also concluded that when the rotational ratio reaches to its critical value of 2, the vortex shedding process vanishes.

Ezadi Yazdi and Bak Khoshnevis [19] investigated the effect of the gap ratio and Reynolds number on the characteristics of the flow around an elliptical cylinder. In their investigation, the Reynolds number was considered to be 13250 and 26500 and gap ratio was in the range of 0 and 2. Their results showed that by increasing the gap ratio, the Strouhal number rises. Moreover, in another study [20], they evaluated the higher-order central moments of velocity signals in the plain wake behind a circular cylinder. They provided new relationships for higher-order central moments such as *skewness* and *kurtosis*, which were more accurate than theoretical relations of other researchers.

Chen and Rheem [21] investigated the flow around a rotating cylinder experimentally. They changed the dimensionless spin ratio (α) from 0 to 8 and investigated the effect of aspect ratio and Reynolds number on hydrodynamic coefficient and Strouhal number of a rotating cylinder. They found that the critical transient region lies $1 \times 10^5 \leq \mathrm{Re} \leq 1.59 \times 10^5$ in range.

Large-eddy simulation (LES) was conducted by Lehmkuhl *et al.* [22] which exhibited the mean-flow separation bubble upstream in the primary-separation zone at supercritical Re. The details of near-surface flow behaviour were described by Cheng *et al.* [23] through the drag crisis utilizing LES.

Karabelas *et al.* [24] studied the turbulent flow past a rotating cylinder for high Reynolds numbers. They found the decrease of drag coefficient by increase of the spin ratio. Furthermore, Cheng *et al.* [25] addressed turbulent flow at the vicinity of a rotating cylinder for high Reynolds numbers through use of LES method. Based on their studies, smooth and continuous decline of drag coefficient was observed for the Reynolds number of 5×10^3, whereas $\mathrm{Re} = 6 \times 10^4$, C_D resulted in relatively steep reduction in drag coefficient at $\alpha \sim 0.6$.

Aljure *et al.* [26] used a direct numerical simulation to examine the rotational ratio effect on the characteristics of the flow around a cylinder. They presented their results in the Reynolds number of 5000 and the rotational ratio of $0 \leq \alpha \leq 5$ and showed that for the high rotational ratio, the formed recirculation region behind the cylinder disappears.

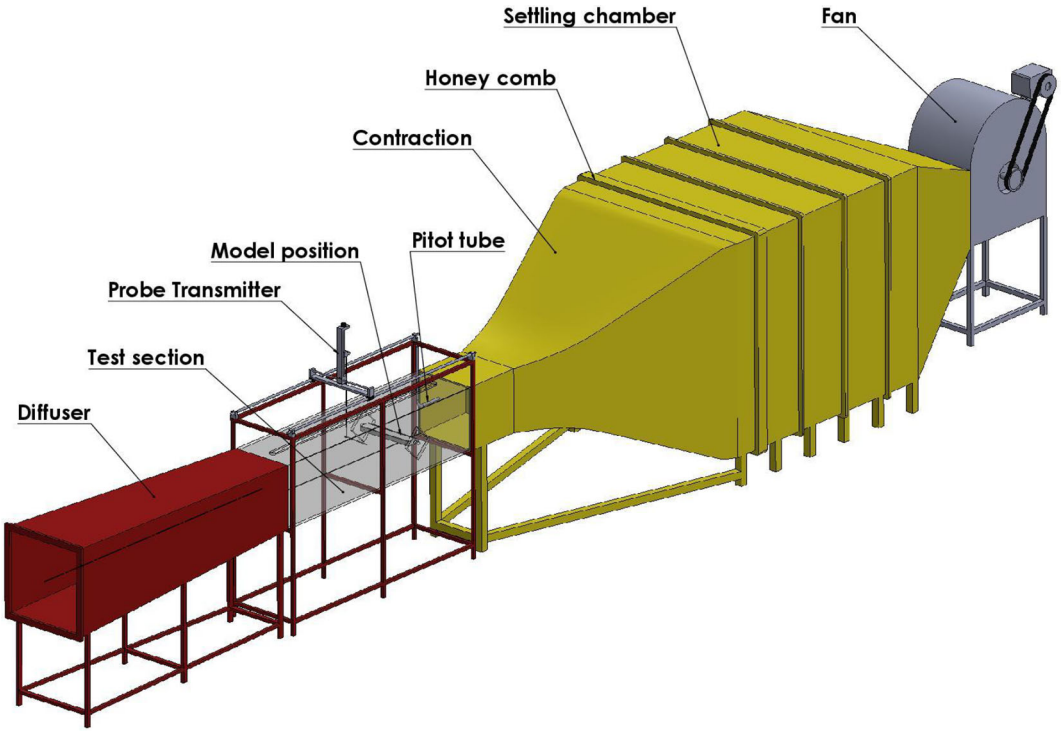

Fig. 1. Experimental facility.

Smaism *et al.* [27] conducted experimental and theoretical investigation about the effect of the rotational ratio on the drag and lift forces in Re = 80, 120 and 160 and $0 \leq \alpha \leq 6$. According to their results, by increasing α up to 4, the drag coefficient decreases, but for $\alpha > 4$, the drag coefficient increases. Also, the lift coefficient has increased with increasing α in all ranges.

By reviewing the related articles, it is found that only few experimental and numerical studies have been carried out simultaneously in the turbulent regime. Since there was not sufficient investigation on the subcritical flow characteristics across rotating cylinder, especially on the lower Reynolds numbers and lower spin ratios, and also, the conducted numerical researches were mainly in a laminar flow, the current study is aimed to fill the gap in this field and investigate the effects of the dimensionless spin ratio on the flow characteristics and the forces applied to the cylinder in the Reynolds number of $5900 \leq \mathrm{Re} \leq 11800$ and the spin ratio of $0 \leq \alpha \leq 0.525$, both experimentally and numerically. Also, no particular information is available on higher-order central moments of velocity fluctuations in the wake of a rotating cylinder, and only a few investigations have been reported the higher-order central moments of velocity fluctuations in the wake of a stationary circular cylinder. Therefore, one of the main goals of this paper that distinguishes it from other published articles is the physical discussion of higher-order statistical quantity (*skewness* factor) and their comparison in different spin ratios and Reynolds numbers. In the present study, new results have been presented regarding the effect of cylinder rotation on the mean velocity profiles, turbulence intensity, skewness factor, Strouhal number, drag coefficient and its relation with flow patterns.

2 Experimental setup and measurement technique

In this paper, all tests and measurements are carried out experimentally using a blowing type wind tunnel, which is an open-circuit subsonic wind tunnel and located in the mechanical engineering department of Hakim Sabzevari University. In fig. 1 the experimental wind tunnel is depicted. The tunnel is a chamber with a cross section of $400 \times 400\,\mathrm{mm}^2$ and length of 1680 mm, which is used for studying the two-dimensional flows over an elliptic cylinder and the results are provided in [28]. The velocity of the air in the test section can be varied between 0 and 30 m/s using a new frequency inverter, the rotational speed of the cylinder is in the range of 0 and 3000 rpm with the same flow velocity. After examining and testing few motors, including step motors, gearbox motors and AC electromotor, an electromotor with output of 1,450 rpm and power of 3-horsepower is selected for providing the cylinder rpms. To provide different cylinder rpms, an inverter or a transmission mechanism with a change in the diameter of the two axles (engine axle diameter and cylinder axle) can be used. Due to the convenience and affordability, in this paper, a pulley and belt mechanism is used to provide a different rpms of cylinders. The mentioned mechanism contains pulleys of different

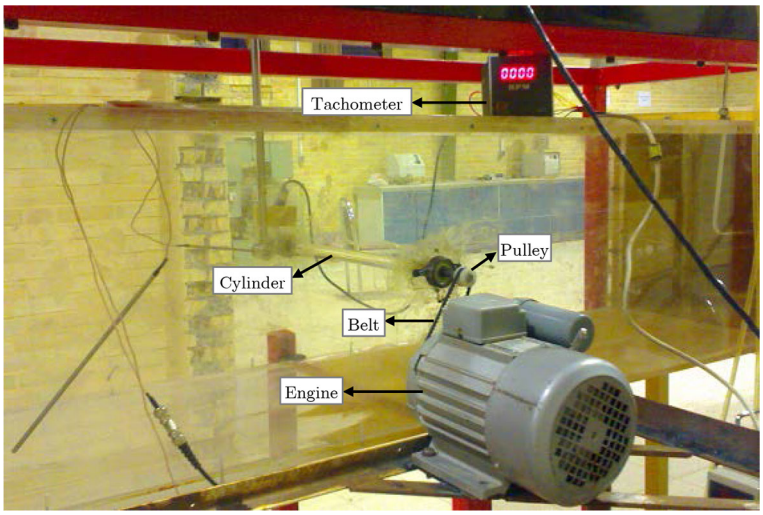

Fig. 2. Cylinder rotation in the test section.

diameters; however, the diameter of the motor's pulley is fixed. The diameter of the motor's pulley is 40 mm and the diameters of the cylinder's axle are 20, 24, 30, 40 and 60 mm. Considering the chosen size for the pulleys in this study, the cylinder can be revolved with a rotational speed of 500, 1000, 1500, 2000, 2500 rpm. To measure the rotational speed of the cylinder, a digital tachometer is used, which indicates the rotational speed of the cylinder in terms of rpm in each moment. Figure 2 shows the engine, belt and pulley, cylinder, and tachometer. The tested circular cylinder is made of Plexiglas, so the effects of surface roughness can be ignored in the results. The diameter of the cylinder is 20 mm with the blockage ratio of approximately 5% in the tunnel, which can be considered negligible, therefore no correction is required for the measured free stream velocity. The span (W) of the cylinder is considered to be 400 mm, so, according to the diameter of the cylinder, the aspect ratio, which is defined as the ratio of the cylinder span to its diameter (W/D), is obtained 20. The obtained aspect ratio is large enough to guarantee a two-dimensional flow in the central region of the near wake. For free stream velocities of 5, 8 and 10 m/s and the mentioned cylinder diameter, Reynolds numbers are in the range of $5900 \leq \mathrm{Re} \leq 11800$.

Experiments are conducted with a hot-wire anemometer, also, a three-dimensional traversing mechanism constructed by Fara Sanjesh Saba Co. (FSS) is used for precise positioning the hot-wire probe, through which stream-wise and span-wise motions as well as the vertical motion in the tunnel can be achieved. The profile of the flow velocity and turbulence intensity in the downstream of the model are measured by a hot-wire sensor, from FSS Co., which can be seen in fig. 3. The type of the hot-wire probe is single normal (SN) and the sensor is made of tungsten wire with a diameter of 5 μm. In addition, the sampling frequency of the hot-wire anemometer (HWA) and its probe is 5 kHz.

The existing uncertainties in the measurement of drag coefficient are due to the uncertainty in measuring the instantaneous velocities and the uncertainty in the positioning of the hot-wire probe. By assuming a Gaussian distribution with a coverage factor of 2, the uncertainty can be obtained according to table 1 [29].

According to that table, the total uncertainty in measuring the velocity using HWA is about 1.57%.

3 Description of the numerical model

In the RANS (Reynolds averaged Navier-Stokes) approach, by substitution of the Reynolds decomposition into the Navier-Stokes equation, the continuity and momentum equations are obtained as follows:

$$\frac{\partial u_i}{\partial x_i} = 0, \tag{1}$$

$$\rho\left(\frac{\partial u_i}{\partial t} + \frac{\partial u_i u_j}{\partial x_j}\right) = -\frac{\partial p}{\partial x_i} + \frac{\partial}{\partial x_i}\left(\mu\left(\frac{\partial \mu_i}{\partial x_j} + \frac{\partial u_j}{\partial x_i} - \frac{2}{3}\delta_{ij}\frac{\partial u_l}{\partial x_l}\right)\right) + \frac{\partial}{\partial x_i}\left(-\rho\overline{u_i' u_j'}\right), \tag{2}$$

in which, u_i and u_j are mean velocities, u_i' and u_j' represents fluctuating part of velocity, δ_{ij} indicates the kronecker delta function, p is the dynamic pressure and ρ is the fluid density. These equations contain an unknown Reynolds stress tensor ($-\rho\overline{u_i' u_j'}$) term, which describes an open set of equations. To close the system, several approaches can be used; a common approach is the use of Boussinesq approximation, which is defined as

$$-\rho\overline{u_i' u_j'} = \mu_t\left(\frac{\partial u_i}{\partial x_j} + \frac{\partial u_j}{\partial x_i}\right) - \frac{2}{3}\left(\rho k + \mu_t\frac{\partial u_k}{\partial x_k}\right)\delta_{ij}. \tag{3}$$

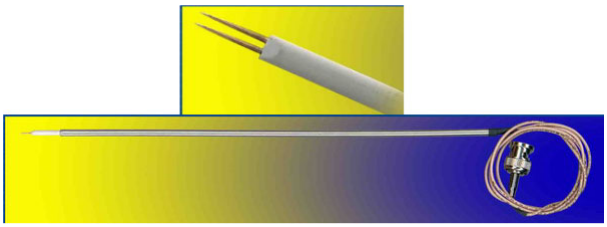

Fig. 3. Hot-wire sensor.

Table 1. Considered uncertainty in the tests.

Type of uncertainty	Uncertainty value (%)
Uncertainty in velocity measurements ($U > 2.5\,\mathrm{m/s}$) using pitot tube and pressure transducer	0.006
Uncertainty in the traverse mechanism	0.003
Uncertainty in the A/D board resolution for 12 bit and 10 V	0.0007
Uncertainty in the ambient temperature variations	0.002
Uncertainty in spline curve fitting	0.004

Note that in the above equation, μ_t is the turbulent viscosity and k is the turbulence kinetic energy. In order to obtain the turbulent viscosity, μ_t, some additional transport equations should be solved, the number of which is dependent on the selected turbulence model. In this paper, the k-ω SST turbulence model is selected and its priority over two-equation turbulence models (k-ϵ model and k-ω model) is mentioned.

3.1 The k-ω SST model

The k-ω SST model [30] benefits from the advantages of k-ω model and k-ϵ model in near-wall region and in far-field region, respectively. In this procedure, the k-ϵ model is transformed to into a k-ω formulation and the blending function is incorporated in the near-wall and far-field regions.

So, wide range of flow profiles with acceptable accuracy can be modeled using the k-ω SST model. The transport equations are as follows:

$$\frac{\partial}{\partial t}(\rho k) + \frac{\partial}{\partial x_i}(\rho k u_i) = \frac{\partial}{\partial x_j}\left[\Gamma_k \frac{\partial k}{\partial x_j}\right] + \tilde{G}_k - Y_k, \tag{4}$$

$$\frac{\partial}{\partial t}(\rho \omega) + \frac{\partial}{\partial x_i}(\rho \omega u_i) = \frac{\partial}{\partial x_j}\left[\Gamma_\omega \frac{\partial \omega}{\partial x_j}\right] + \tilde{G}_\omega - Y_\omega + D_\omega, \tag{5}$$

where G_k/G_ω, Y_k/Y_ω and Γ_k/Γ_ω are the production, dissipation and effective diffusivity terms for k and ω, respectively, and finally D_ω represents the cross-diffusion term. A blending function, F_1, deals with production, dissipation, diffusivity and cross-diffusion terms and defined as follows:

$$\phi = F_1 \phi_1 + (1 - F_1)\,\phi_2 \tag{6}$$

where ϕ_1 and ϕ_2 contain the constants in the original k-ω model and transformed k-ϵ model, respectively. ϕ represents the overall constants of the model and F_1 represents the blending function, which is equal to 1 in the near-wall region and it is equal to 0 in far-field region. For more detailed description of the k-ω SST model and the blending function the reader is referred to Menter [30].

3.2 Computational domain and boundary conditions

The computational domain and the details of the grid in simulation process are depicted in fig. 4. As can be seen in fig. 4(a), the cylinder diameter, which is denoted by "D" in the figure, is 20.00 mm, which is selected to be the same as the diameter of the model in the experimental tests. The distance between the flow inlet and the cylinder center is selected to be 12.5 times of the cylinder diameter ($12.5D$). The length scales in the X- and Y-directions of

the computational domain are considered to be $55D$ and $20D$, respectively, which are sufficiently large to guarantee the fully developed flow. The whole computational domain is divided into 12 sections. As can be seen in fig. 4(b), in the areas that are labeled from 1 to 4 in the vicinity of the cylinder, fine grids are used. Regarding fig. 4(c), for avoiding the effects of the wall, extremely fine grids are used in the boundary layer in the vicinity of the walls. For the remaining sections, the length of the grids increases in the radius direction and are coarser compared to the grids in the 1 to 4 sections. By using this type of gridding, the calculation costs can be decreased due to the use of coarser grids in the far regions and the accuracy of the simulations can be guaranteed due to the use of finer grids near the wall region. In all simulations, structured mesh is used. In the inner region and in the cylinder wall, the grid expansion ratio are varied between 1.01 and 1.05. In the outer region, the grid expansion ratio is constant and it is equal to 1.02 for the downstream and is equal to 1.05 for the far fields (both upper and lower) and upstream. The total number of the cells is 97862.

Uniform velocity and fully developed boundary conditions are considered for the inlet and outlet boundary conditions, respectively. Also, symmetric boundary condition is used for the top-bottom walls. The inlet velocity is considered as the initial velocity and the outlet relative pressure, which is equal zero, is considered as an initial pressure throughout the computational field.

The input parameters for inlet free stream flow are derived from present experimental results, in which the turbulence intensity was $TI = 0.1\%$. In addition, the turbulence viscosity ratio of 1 ($\mu_t/\mu = 1$), which is recommended for external flows, is utilized in the simulations. The turbulent kinetic energy (k), turbulent dissipate rate (ϵ) and specific dissipation rate (ω) can be specified as follows:

$$k = \frac{3}{2}\left(u_{ave} \times TI\right)^2, \tag{7}$$

$$\epsilon = \rho C_\mu \frac{k^2}{\mu}\left(\frac{\mu_t}{\mu}\right)^{-1}, \tag{8}$$

$$\omega = \rho \frac{k}{\mu}\left(\frac{\mu_t}{\mu}\right)^{-1}, \tag{9}$$

where u_{avg} is the mean velocity and $C_\mu = 0.09$ is an empirical constant.

The computational grid has been generated by the ICEM software version 17.1. To check the grid independency, different grid sizes of 4593, 23848, 78798 and 97862 are selected for solving the flow over the stationary cylinder at the Reynolds number of 5900. The drag coefficient is calculated for each grid and the results are compared together (table 2). The comparison of the results showed that by further increase of the grid size over 78798, no significant variation is obtained, so this grid size is selected as the most appropriate grid over the whole investigation.

The FLUENT 17.1 is used for simulations and the solution of the governing equations is achieved by finite volume method (FVM). Also, SIMPLEC scheme is utilized for coupling of the pressure-velocity in all simulations; the remaining schemes for different conditions are as follows: second order implicit scheme for transient formulation; least squares cell-based scheme for gradient discretization, standard scheme for pressure discretization, first-order upwind scheme for momentum discretization, second-order upwind scheme for the k-ω SST model and first order upwind scheme for turbulent kinetic energy and specific dissipation rate discretization.

4 Results and discussion

4.1 Experimental measurements

The measurements of the flow characteristics are conducted using a single hot-wire with the ability of conducting automatic stream-wise and cross-wise motions as well as vertical motion in the tunnel. The origin of the coordinate system is located at center of the circular cylinder. The probe is placed at three locations in the downstream of the circular cylinder and has upward and downward motions. The maximum error for measuring the locations is ± 0.1 mm. In vertical direction of the circular cylinder downstream, 121 points are selected for conducting measurements. For each of the selected points, some measurements are performed and then the obtained values are averaged using Flow-Ware program developed by Fara Sanjesh Saba Co. (FSS). It should be noted that the hardware and all of the components are manufactured by FSS Co. and are depicted in fig. 5.

About 6 hours were spent for each set of measurements in the room temperature of 20 °C with a variation of ± 1 °C during the experiment period. Velocity and the difference between the temperature of the wire and fluid affect the output of constant temperature anemometer, so, the output of the anemometer should be corrected in order to obtain accurate measurement of the flow velocity. In the present paper, the bridge voltages of the anemometer are multiplied with appropriate correction factor to be in a standard reference temperature of 27 °C.

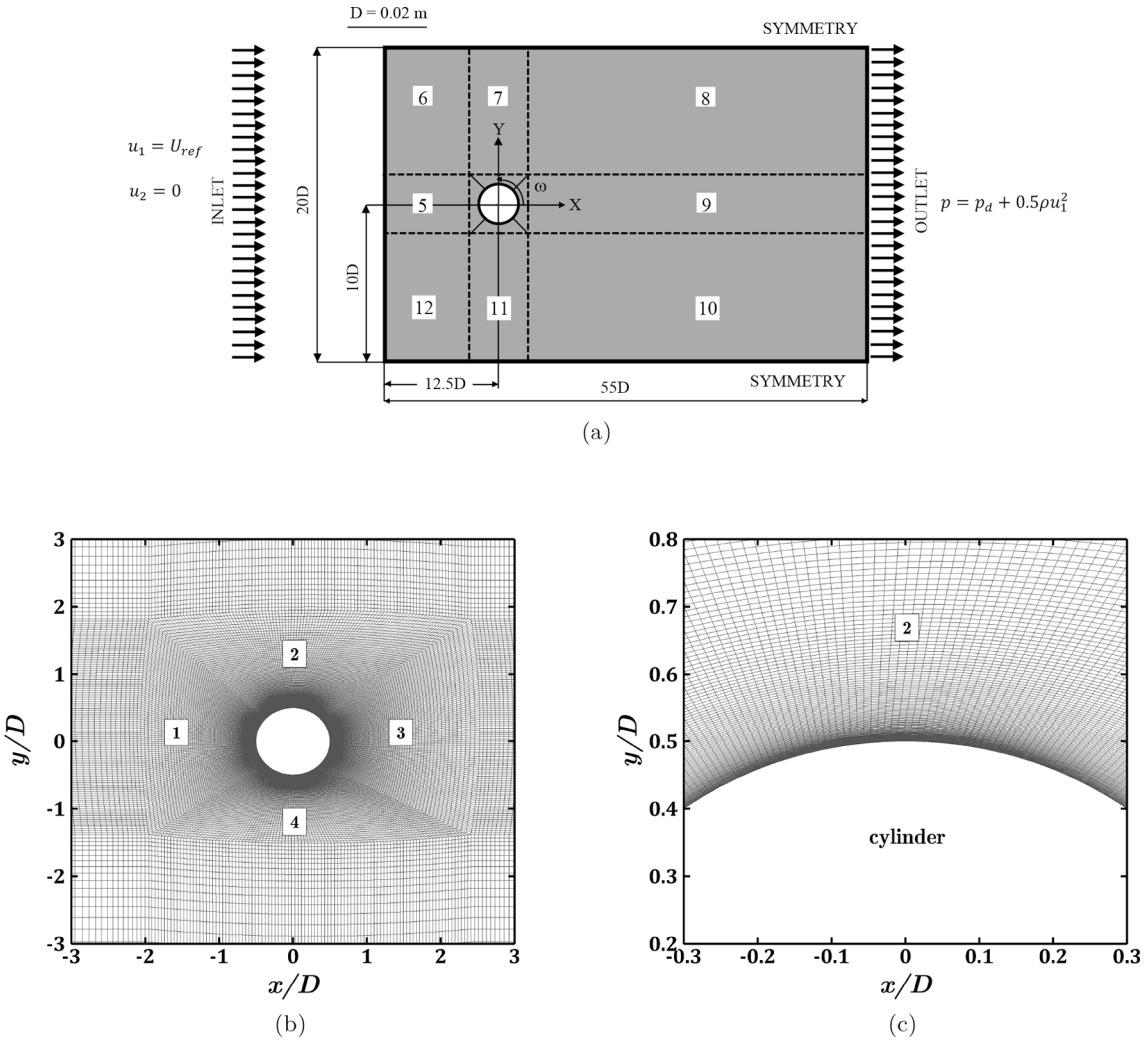

Fig. 4. Schematic of the computational domain and grid details, (a) scale of the computational domain, (b) the grid details near the cylinder and (c) the boundary layer mesh near the cylinder wall.

Table 2. Results of the mesh sensitivity study for the k-ω SST model.

Grid size	C_D
4593	1.356
23848	1.088
78798	1.054
97862	1.045

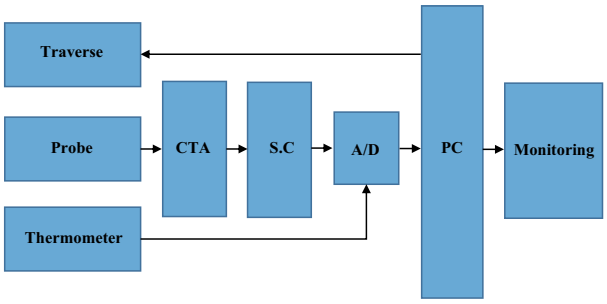

Fig. 5. Arrangement of hardware system and monitoring from FSS Co.

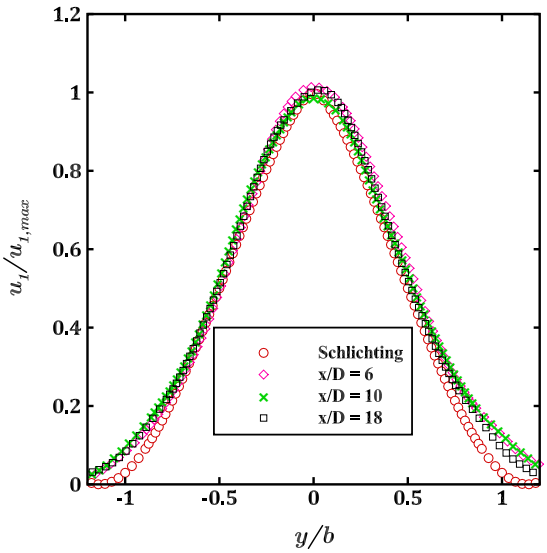

Fig. 6. Velocity profile for $\alpha = 0$ and Re = 11800. Red circles refer to a self-similar solution through Schlichting and Gersten [31].

4.1.1 Time-averaged velocity (u)

Maximum deficit $u_{1,max}(x)$ and its corresponding position $y_{1,max}(x)$ were identified by analysis of the profile of the wake deficit of momentum $u_1(x,y) = u(x,y) - u_{max}(x)$, in which $u_{max}(x)$ represents the maximum local velocity along the wall normal direction. Proper scale of the velocity profiles in the wake is highly dependent on the mentioned parameter [31]. According to the studies on turbulent wakes [32], the wake boundaries $y_{wake}(x)$ refer to sites where $u_1(x, y_{wake})/u_{1,max}(x) = 0.5$. $b(x)$ denotes the wake width defined as the distance between the wake boundaries along the y-direction.

Figure 6 represents the velocity deficit profile for different x-distances relative to cylinder downstream for $\alpha = 0$ and Re = 11800. The velocity deficit profiles coincided on a single curve when y-coordinate was rescaled to the width of the wake (b) while the velocity deficit was rescaled to $u_{1,max}$. Although we can't make sure on self-similarity at such short stream-wise distance ($x/D \leq 6$), the velocity deficit profiles were properly comparable with the theoretical asymptotic results obtained from Schlichting and Gersten [31]:

$$u_1 = u_{1,max}\left(1 - \left(\frac{y}{b}\right)^{\frac{3}{2}}\right)^2. \tag{10}$$

Similar results were obtained in almost all the cases at Re = 5900 and 9400 (not presented here). This can guarantee minimum blockage effects on the attained results. As it can be seen, the results of the current study showed good agreement with Schlichting correlation.

The profiles of the normalized stream-wise mean velocity (u/U_∞) for the specified x/D locations, various spin ratios and different Reynolds number in the range of 5900 and 11800 are shown in fig. 7(a)–(c). The wake width and the center velocity vary largely according to the changes in the mean velocity. As can be seen from fig. 7(a)–(c), a larger velocity defect is developed in $x/D = 1.5$ compared to $x/D = 3$ and $x/D = 6$.

Also for rotating cylinder, the velocity defect is very large at $x/D = 1.5$ compared to $x/D = 3$ and $x/D = 6$. With increasing the values of α and Re, the velocity defect would be decreased. It is apparent that the velocity defect is reduced by increasing the x/D. It was also observed that the width of the velocity defect is larger for rotating cylinder compared to the stationary cylinder. As can be seen in these figures, the rotation of the cylinder increases the velocity inside the vortices and reduces the velocity outside the wake; these changes are more pronounced by increasing the rotational speed of the cylinder. Moreover, with increasing x/D, the velocity difference inside and outside the wake is reduced, which would result in more uniform mean velocity profile due to the increase of the wake width. In the near-wake region, due to presence of separations and recirculating flows, velocity drop is intensified; as the x/D increases, the velocity drop decreases and got more uniform inside the wake. According to the obtained results, it can be concluded that rotation of the cylinder disturbed the symmetry of the wake and the velocity profiles are stretched out over the positive direction of the y-axis, subsequently.

Moreover, by increasing the spin ratio, the separation point was displaced downward. At $x/D = 6$, the velocity profiles are similar but the rotation of the cylinder stretched the velocity profiles in the shear layer of the upper side of the cylinder toward the positive direction of the y-axis.

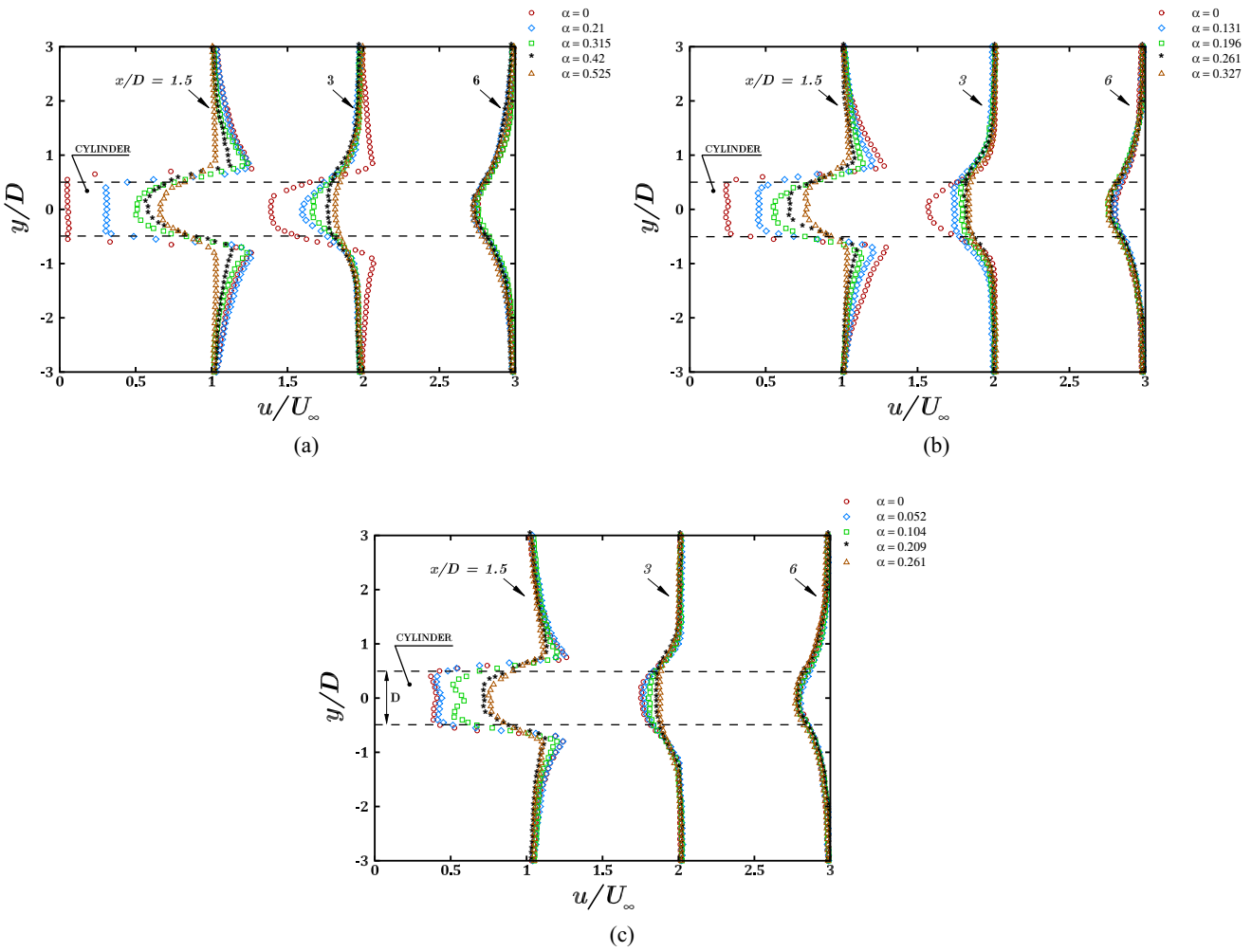

Fig. 7. Time-averaged mean streamwise velocity profiles at three downstream locations ($x/B = 1.5, 3$, and 6) for different spin ratios; (a) Re = 5900, (b) Re = 9400, and (c) Re = 11800.

On the other hand, the wake size (defined as the width of disturbed section in the profile of free stream velocity) and length (referring to the distance at which the flow restores the free-stream velocity value) are highly dependent on rotation. The rotation will decline the rear wake size of the downstream which moves side through a pumping action where the pumped fluid (from the upstream flow) feeds the upper parts of the wake past the cylinder. Such pumping action will also fill the wake with the pumped fluid earlier, thus, inducing shorter wakes.

The deficit velocity (U_w) is defined by the difference between the free-stream and the minimum velocity on the wake centerline. The parameter of deficit velocity is illustrated in fig. 8. Figure 9 shows the non-dimensional deficit velocity parameter in terms of α at specified x/D locations. The results show that in $x/D = 1.5$ and 3, with increasing α, the parameter of deficit velocity decreases. In $x/D = 6$, with increasing α, the parameter of deficit velocity increases or decreases depending on the value of α. Due to the change in the mean velocity profiles, there is no specific trend for the value of the deficit velocity parameter in this position. It can be seen that with increasing of Re, the parameter of deficit velocity decreases.

4.1.2 Relative turbulence intensity (TI)

The turbulence intensity *versus* different spin ratios is depicted in fig. 10(a)–(c) for three positions in the x-direction. Two main peaks can be observed in the profiles of turbulence intensity at selected x/D locations according to the transitional state of the shear layers. Shear layer flapping is suggested for the possible cause of these peaks as the results of the shear layer inflection by the initial formation of the vortex. As shown in fig. 10(a) and at $x/D = 1.5$ for $\alpha = 0 - 0.315$, in the regions between the two peaks the flow is comparatively quiet; however, it becomes strongly agitated in the place of initial vortices generation at the end of recirculation area. There is also a phenomenon in

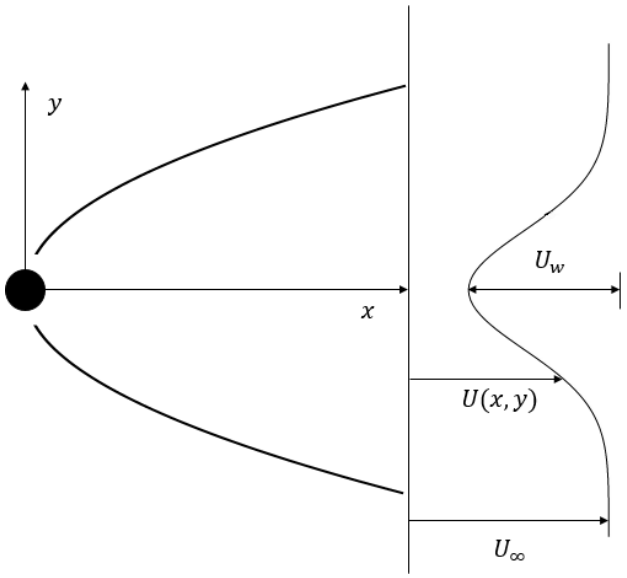

Fig. 8. The parameter of deficit velocity.

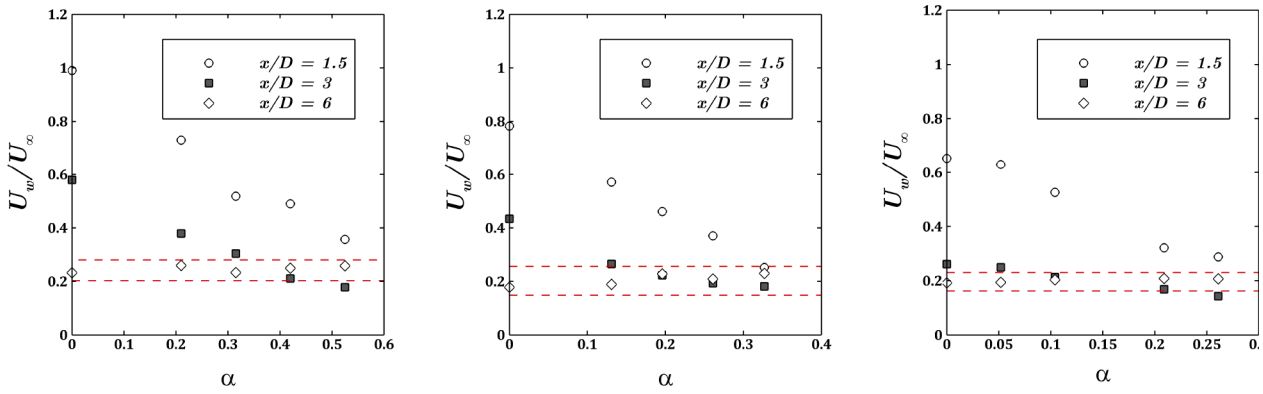

Fig. 9. Variation of the normalized velocity defect in terms of α for various x/D locations; (a) Re = 5900, (b) Re = 9400, and (c) Re = 11800.

Reynolds numbers 9400 and 11800. The results showed that by increasing the cylinder rotational speed, the turbulence intensity is enhanced. By analyzing the results in different rotational speeds, it is found that the diagram of the turbulence intensity has two maximum values near the wake boundary; however, for higher velocities ($\alpha = 0.42$ and 0.525), another maximum value can be observed at the wake center, which can be resulted from the variations in the vortices formed behind the cylinder. It is also apparent that the maximum shear stress is occurred in the regions outside the wake center. Another important point that can be figured out from these diagram is the dependency of the turbulence intensity to the distance from the cylinder; as the distance increases, the turbulence intensity in and around the boundary of the cylinder wake first has an increasing trend and then decreasing trend; at the distances far away from the cylinder, the turbulence intensity becomes constant. This trend is due to the presence of separations and recirculating flows near the cylinder and uniform flows at the further distances. Regarding the vortices behind the cylinder, the turbulence intensity decreased by increase of cylinder rotational speed at $x/D = 3$, which is in contrast to the turbulence intensity diagrams obtained in the previous position. The turbulence intensity diagram of the rotating cylinder at $x/D = 6$ for $\alpha = 0.21$ and 0.315 shows that, in comparison with the stationary cylinder, the turbulence is decreased, while it is increased for $\alpha = 0.42$ and 0.525.

According to turbulence intensity diagram in previous situations, it can be concluded that increasing the rotational speed of cylinder at $x/D = 6$ results in an increase in the turbulence intensity. In this situation, unlike the other diagrams, the turbulence intensity diagrams represents similar behavior in different rotational speeds. Figure 10(b) depicts the turbulence intensity diagram for different α values at $x/D = 1.5, 3$ and 6 in Reynolds number of 9400.

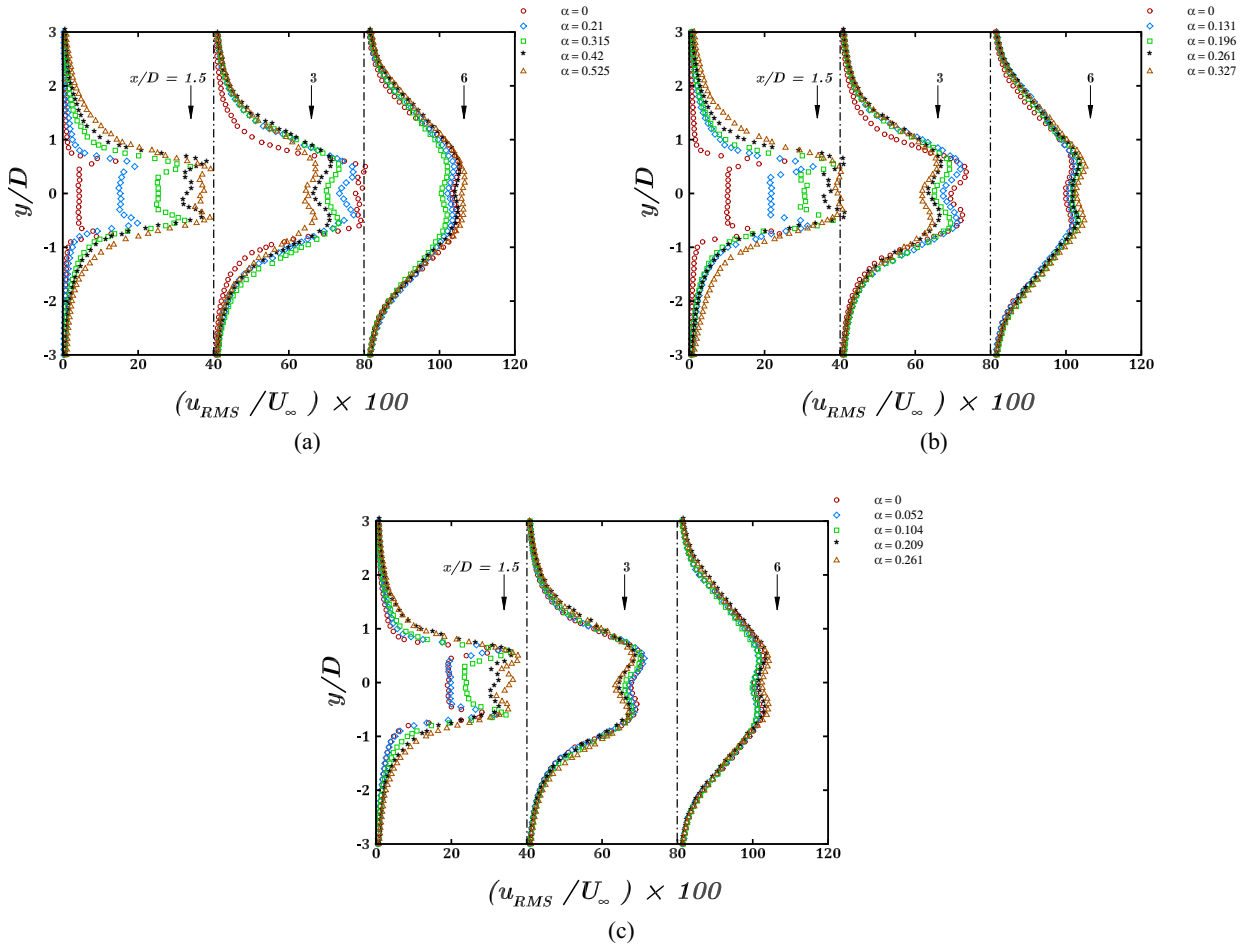

Fig. 10. Turbulence intensity profiles at three downstream locations ($x/B = 1.5, 3$, and 6) for different spin ratios; (a) Re = 5900, (b) Re = 9400, and (c) Re = 11800.

According to this figure, elevating the cylinder rotational speed leads to an increment in turbulence intensity, which is higher compared to that of in Reynolds number of 5900. In the case of stationary cylinder and at low rotational speeds ($\alpha = 0.131$), the turbulence intensity diagram has two maximum values near the wake boundary; but for higher speeds ($\alpha = 0.196, 0.261, 0.327$), another maximum can be seen in the profile of turbulence intensity at the wake center due to the changes in the vortices formed behind the cylinder. As was explained for the velocity profile at $x/D = 1.5$, the turbulence intensity is also stretched over the positive values of the y-axis due to cylinder rotation. At $x/D = 3$, with increase of the rotational speed, the turbulence intensity inside the wake is decreased, unlike the case of $x/D = 1.5$. For $x/D = 6$, increase of rotational speed leads to an increase turbulence intensity.

Figure 10(c) shows the turbulence intensity diagram for different α values at $x/D = 1.5, 3$ and 6 in Reynolds number of 11800. The results of these experiments are similar to those obtained for Reynolds number of 5900; however, due to the increased air velocity and lower rotational speeds, the turbulence intensity in the wake showed about 10% reduction.

Striking results can be obtained by studying the trend of variation in the velocity field through examining the velocity fluctuations in the curves representing the near-wake edges. These variations are depicted in fig. 11(a)–(c) for the upper and lower curves in the horizontal plane under various Reynolds numbers and spin ratios, respectively. The significance of these trends lies in the fact that the fluctuations variations are related to the shear layer instability —hence, the dynamics of the resultant vorticity concentrations— and they could well identify these variations. As fig. 11(a)–(c) suggests, upper wake edge analysis in the horizontal plane revealed that the fluctuations initiated to increase at a certain point which coincided with the onset of instability along the recirculation region boundary. The impact of α enhancement can be then observed as a delay in fluctuations rise, and hence the corresponding upstream movement of the shear layer instability. This is associated with the recirculation region shrinkage. Concerning the lower-side edge of the horizontal plane (fig. 11(a)–(c)), it can be seen that the variation trend is identical to that

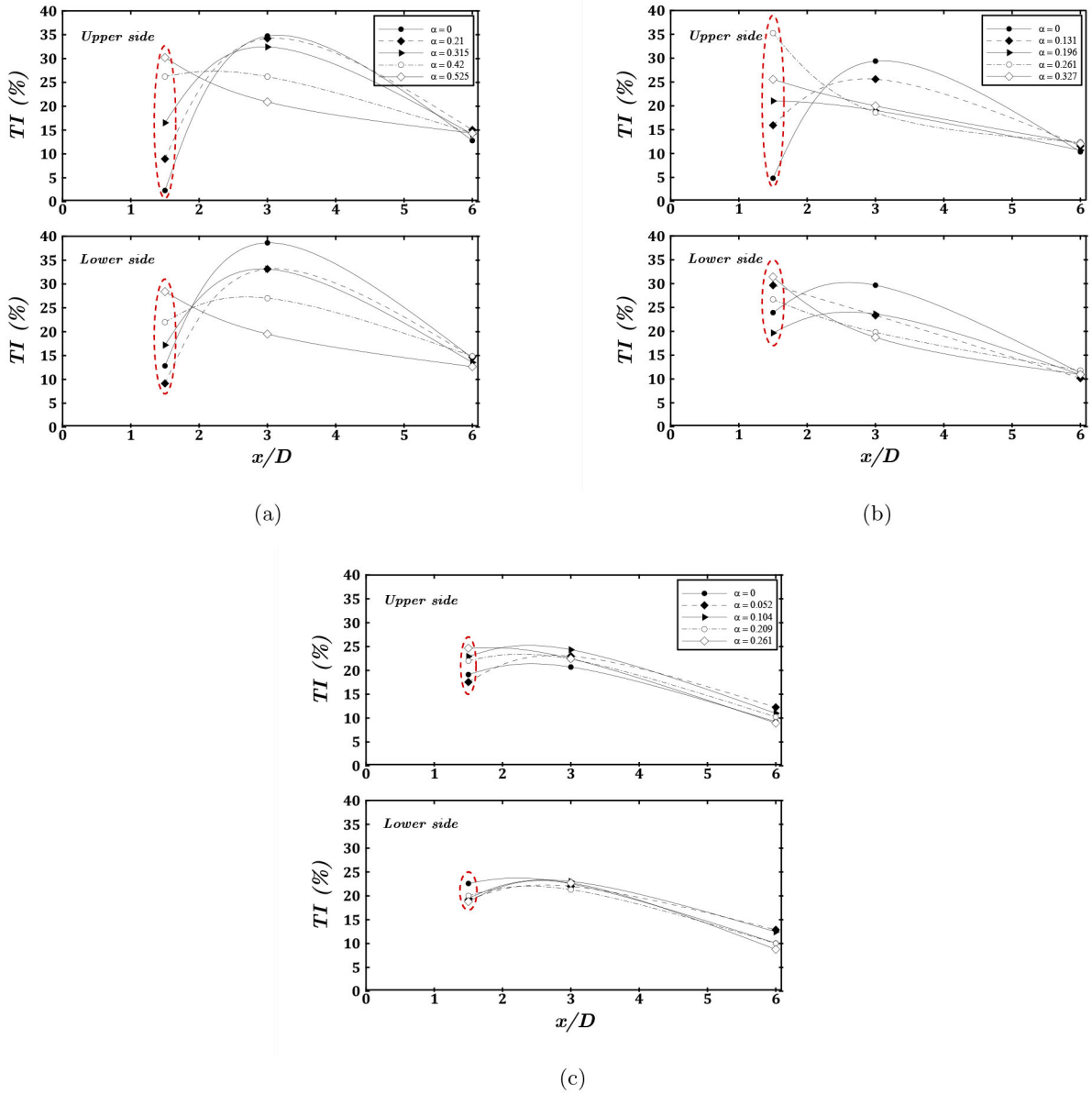

Fig. 11. Variation of the turbulence intensity along the near wake edges. (a) Re = 5900, (b) Re = 9400, and (c) Re = 11800.

observed for the upper-side edge. Moreover, higher upstream fluctuations values were observed along the mentioned curve (Re = 5900 at $\alpha = 0.525$; Re = 9400 at $\alpha > 0.196$), again it can be attributed to the rotational movement of the cylinder. At Re = 11800, the trend were identical along the upper and lower side edges (fig. 11(c)) they however showed smaller and delayed variations.

As shown in figs. 12–14, the reduction of the wake width can better be appreciated from the analysis of the velocity fluctuation averaged in the stream-wise direction. Turbulence intensity in the near wake presents two peaks of maximum fluctuation (see figs. 12–14). These points are connected with the vortex formation length [33–35]. Turbulence intensity (the root-mean-square of the fluctuating velocity) contours for $0 \leq \alpha \leq 0.525$ and Re = 5900 in terms of free stream velocity are presented in fig. 12. As can be seen in fig. 12(a)–(c), by increasing the x/D in the range of $2.5 < x/D < 4.5$, the turbulence intensity reaches to a maximum value in the wake region before decaying.

The turbulence structure experiences substantial changes with increasing α; however, it seems symmetric with respect to the wake center ($y/D = 0$) with increasing α up to 0.315. With increasing α from 0.42 to 0.525, the asymmetry in the turbulence structure grows. It was also observed that up to $\alpha = 0.315$, the turbulence intensity is reduced in the shear layer of the upper and lower cylinder surfaces but it is increased at $\alpha > 0.42$.

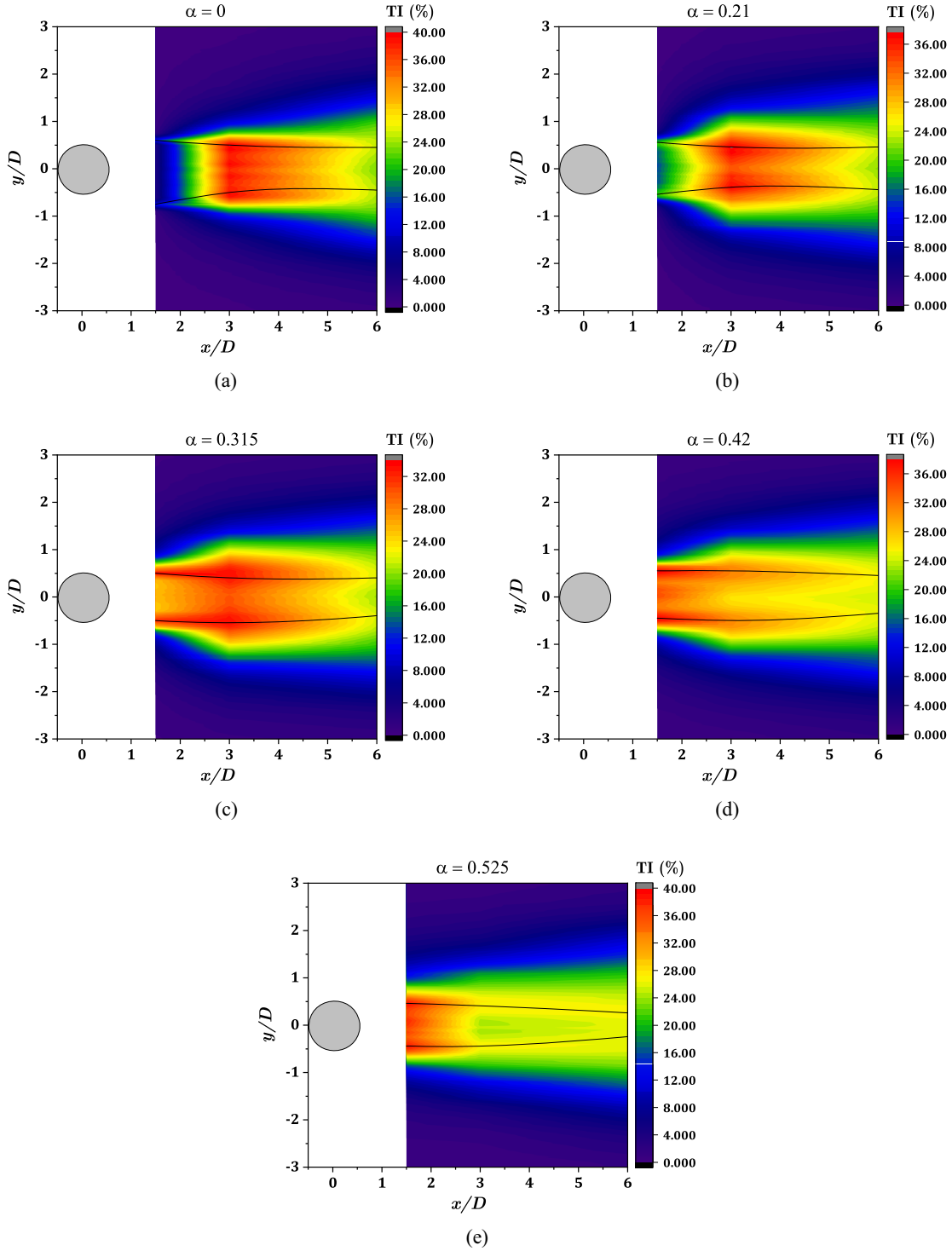

Fig. 12. Turbulence intensity contour for various dimensionless ratio (Re = 5900) and points of maximum fluctuation in the streamwise locations (continuous line).

Turbulence intensity contours for $0 \leq \alpha \leq 0.327$ and Re = 9400 are presented in fig. 13. The turbulence intensity is symmetric with respect to the wake center ($y/D = 0$) at $\alpha = 0$. With increasing α, the asymmetry in the turbulence structure grows. It is seen that the turbulence intensity increased in the shear layer of the upper and lower surfaces of the cylinder. In Re = 9400, the turbulence intensity is increased with increasing α, compared to Re = 5900.

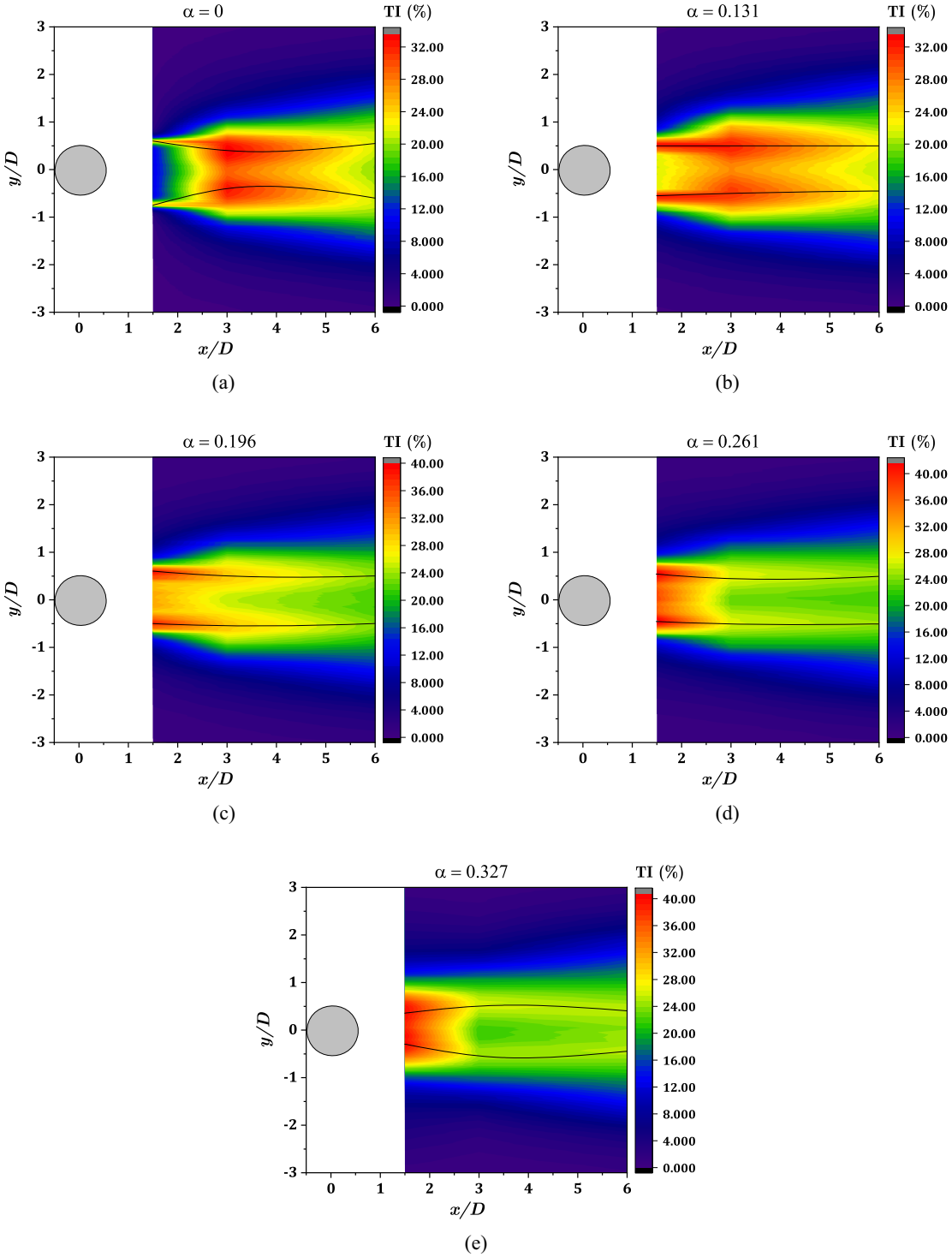

Fig. 13. Turbulence intensity contour for various dimensionless ratio (Re = 9400) and points of maximum fluctuation in the streamwise locations (continuous line).

Turbulence intensity contours for $0 \leq \alpha \leq 0.261$ and Re = 11800 are presented in fig. 14. Just like what is seen in other Reynolds numbers, the symmetric profile of the turbulence intensity with respect to the wake center ($y/D = 0$) can be seen at $\alpha = 0$. At Re = 11800, with increasing α, $TI\%$ at the shear layer of the cylinder is increased. The turbulence intensity in the upper shear layer of the cylinder at spin ratio of 0.052, 0.104, 0.209 and 0.261 are higher compared to $\alpha = 0$.

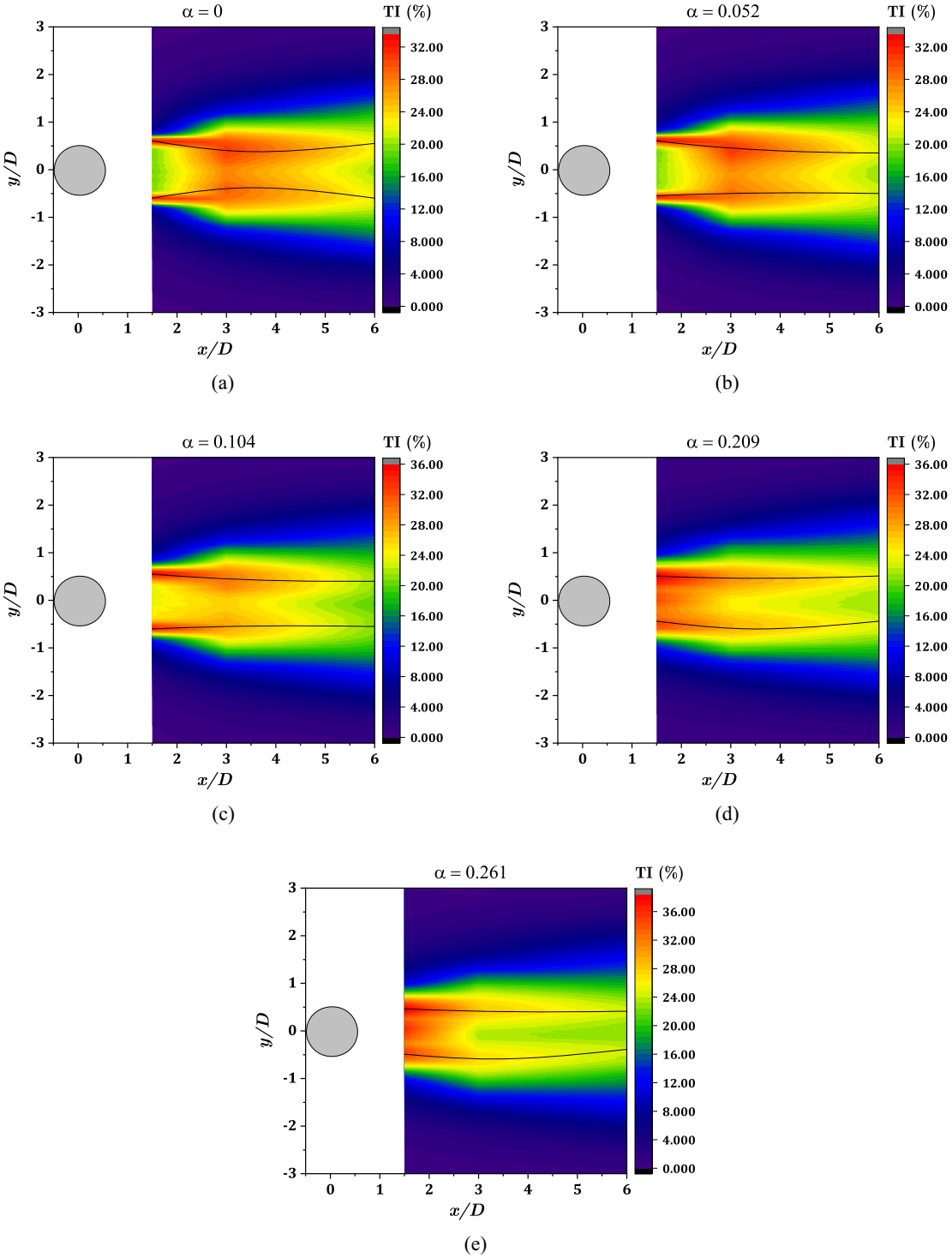

Fig. 14. Turbulence intensity contour for various dimensionless ratio (Re = 11800) and points of maximum fluctuation in the streamwise locations (continuous line).

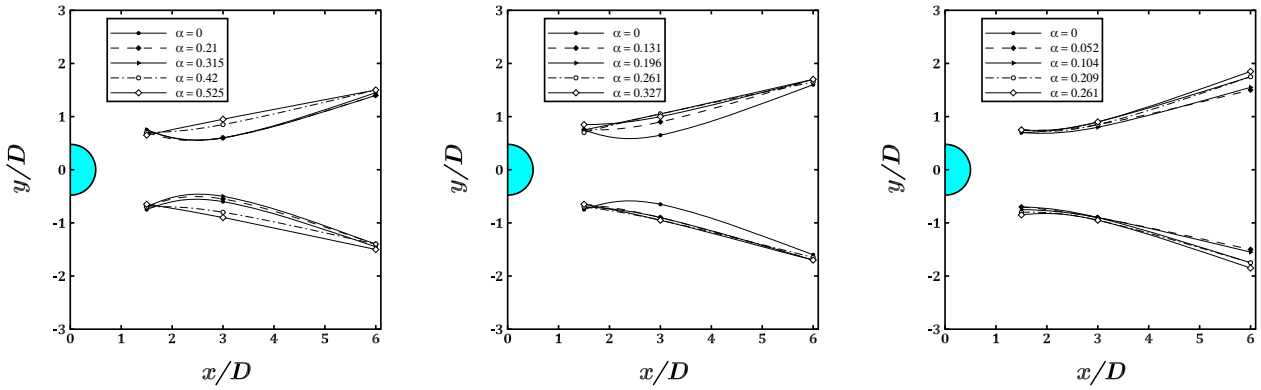

Fig. 15. Effect of the variation of the spin ratio and Reynolds number on the near wake flow features. (a) Re = 5900, (b) Re = 9400 and (c) Re = 11800.

4.1.3 Higher-order central moments

The skewness refers to the dimensionless third-order central moments normalized by the third power of the standard deviation showing a peak at the outer zone. It is expected since the mentioned peaks were previously reported at the boundary of turbulent regions possessing high mean shear (for more details, see Wygnanski and Fiedler [36] who addressed a general two-dimensional mixing region, Fabris [37] and Mariotti *et al.* [38–40] investigating the wakes, Antonia and Krogstad [41] who studied boundary layers, and Buresti *et al.* [42] who examined the jets).

Figure 15(a)–(c) illustrates the horizontal plane representation of wake edges (points of minimum skewness) under various Reynolds numbers and spin ratios. Figure 15(a) reveals that for the case with $\alpha = 0$ to 0.315, the wake width first declined and reached to a minimum value; which may be associated to the end of the mean recirculation region.

Such decline was not observed in spin ratios of 0.42 and 0.525 reflecting a reduction in the length of mean recirculation region and hence drag coefficient. As fig. 15(b) suggests, for $\alpha = 0$, the wake width first decreased and reached to a minimum which may be associated to the end of the mean recirculation region. Such decline was not observed for enhanced spin ratios reflecting a reduction in the length of mean recirculation region and hence drag coefficient (fig. 21). Figure 15(c) also shows a decrease in the length of mean recirculation region by increase of Reynolds number even at $\alpha = 0$ which resulted in shrinkage of wake as can be seen in velocity contours.

In addition to expectable wake shrinking, the declined length of the recirculation region is the most prominent impact induced by enhancement of the spin ratio.

4.1.4 Frequency analysis of the wake velocity signals

Hot-wire sensor received the fluctuations in fluid flow of a wind tunnel in the form of fluctuation *vs.* time (temporal domain). Using its Fourier transform, they can be converted to frequency domain and displayed as fluctuations *vs.* frequency on the screen. In the studied wind tunnel, maximum data collection frequency was 5 kHz. In frequency domain, the entire fluctuations (with various frequencies) of the flow (measured by the sensor) can be observed. Among all the flow fluctuation behind the model, Kármán vortex fluctuations have the highest amplitudes. Therefore, the frequency of the maximum amplitude is in fact the Kármán vortex frequency.

The frequencies were presented in dimensionless forms by a Strouhal number on the basis of the model diameter and free-stream velocity, $St = fD/U_\infty$. Figure 16 compares Strouhal numbers corresponding to the dominating frequencies for 5 different spin ratios. According to Diaz *et al.* [43] and Chew and Cheng [18] St enhancement led to increase of rotation rate which was also supported by other researchers including Jaminet and Van Atta [44], Mittal and Kumar [16], Kumar and Cantu [45] and Kang and Choi [46] who reported decline of St decreases by increase of α.

As fig. 16(a) suggests, increase of α enhanced Strouhal number which is in line with the previous studies. Enhancement of Reynolds number led to almost constant Strouhal number despite increase of α (fig. 16(b) and (c)). It must be mentioned that simultaneous increase of Reynolds number and spin ratio will decline the Strouhal number.

Further understanding on flow development in the near wake regions could be possible by studies aimed to determine the connection of frequency variation with other flow parameters. Interestingly, in recirculation region downstream, the velocity profiles of the various configurations will be identical if presented in terms of suitably chosen non-dimensional coordinates. Concerning the cross sections at a longitudinal coordinate x/D in the horizontal plane, u_{cl} can be defined as the wake center velocity while u_e refers to the velocity at $y = \beta$ in the wake lateral edge. These values can be determined by the skewness negative peaks. Considering these quantities, the data corresponding to different spin ratios

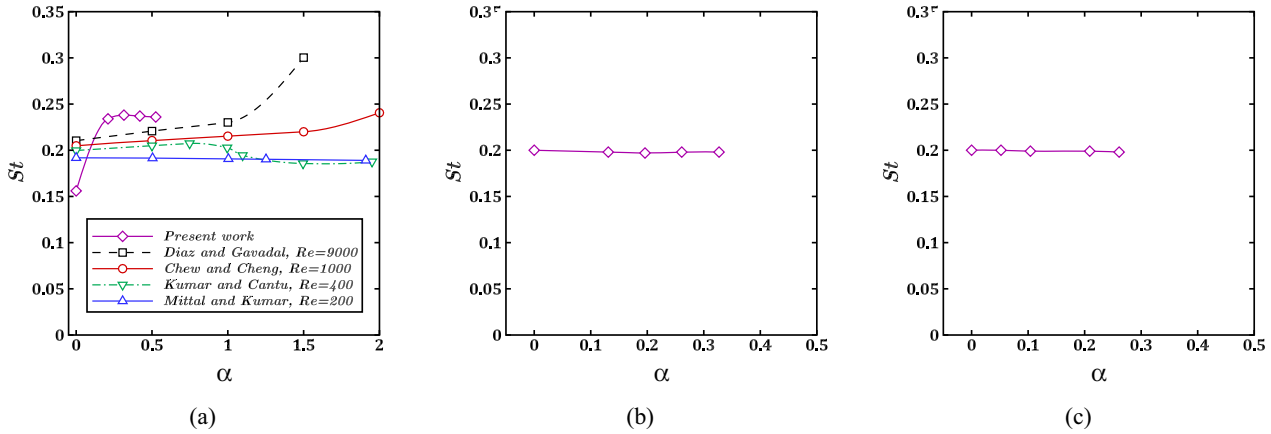

Fig. 16. Variation of the Strouhal number of the velocity signals with spin ratio. The frequencies are measured at $x/D = 3$; (a) Re = 5900, (b) Re = 9400 and (c) Re = 11800.

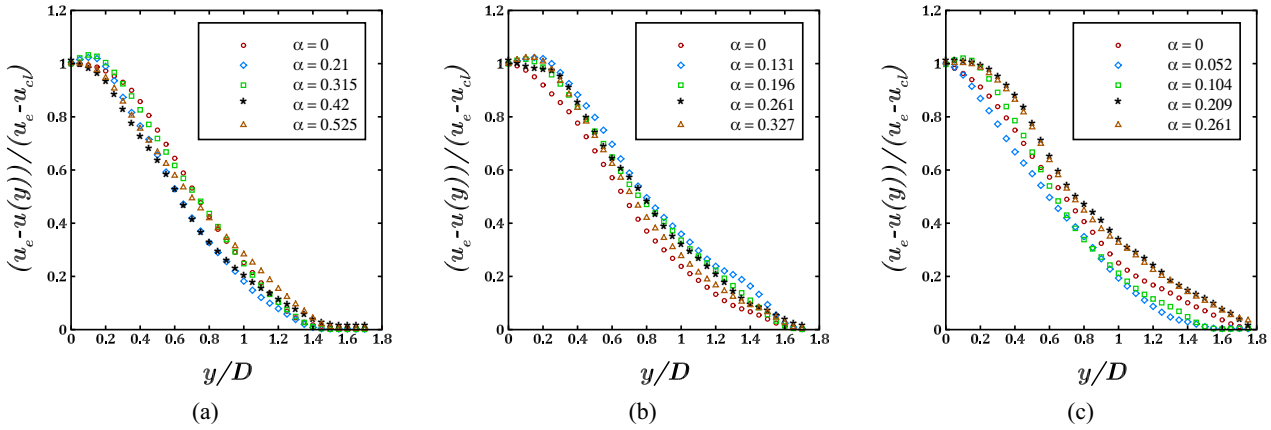

Fig. 17. Non-dimensional velocity defect at $x/D = 6$ as a function of y/D for the different spin ratios; (a) Re = 5900, (b) Re = 9400 and (c) Re = 11800.

will coincide to a single curve when we plot the profile of dimensionless lateral velocity defect $(u_e - u(y))/(u_e - u_{cl})$ *versus* y/D (fig. 17 in which $x/D = 6$). A substantial resemblance was observed in the dimensionless velocity profiles of cross sections beginning from the downstream of recirculation region end; such observations were also reported by Calvert [47] addressing the wakes of several axisymmetric models and by Mariotti and Buresti [38] who examined an axisymmetric blunt-based body.

4.2 Numerical results

Figures 18–20 show the mean stream-wise velocity contours around the stationary and rotating circular cylinder for three spin ratios and Reynolds numbers of 5900, 9400 and 11800. For a stationary cylinder, the flow pattern on the upper and lower sections is symmetrical. The stagnation point at the front and rear of the cylinder is located on the center line and the top and the bottom separation points are almost symmetrical. The vortices are formed alternatively and grow on the upper and lower surface. As can be seen in fig. 18(a), fig. 19(a) and fig. 20(a), the length of the wake area behind the cylinder decreases by increasing the Reynolds number. For rotating cylinder, the flow pattern is no longer symmetrical and the stagnation and separation points are displaced and departed from the centerline. In the case of counterclockwise rotation, a contour-current and a co-current flow on the upper and lower surface of the cylinder are generated, respectively. As a result, the mean velocity is decreased on the upper surface and increased on the lower surface. Hence, there will be a higher pressure on the top surface and a lower pressure on the bottom surface, which creates a downward lift force on the cylinder.

As it is observed, the stagnation points are not on the center line and are displaced upwardly along the surface. The reason is that the tangential velocity of the cylinder surface is added to the flow velocity, which is tangent to the surface, but has an opposite direction on the upper surface. For equal magnitudes of the above velocities, the total velocity will be zero, which occurs at two points on the upper surface. The figure also shows that the wake area behind the cylinder is inclined upward. The reason is that both the separation points are displaced in the direction of rotation; means that on the lower surface, the separation takes place at smaller angels and on the upper surface, it

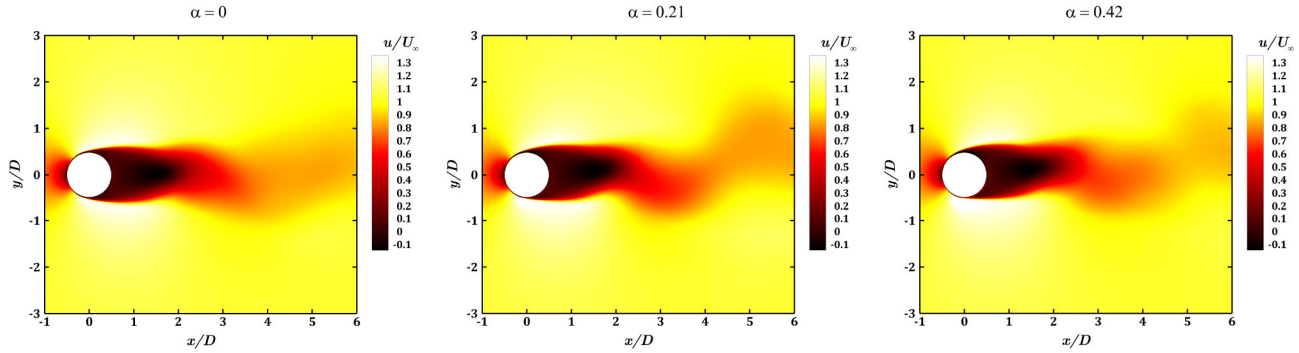

(a) (b) (c)

Fig. 18. Mean stream-wise velocity contour for various dimensionless ratio (Re = 5900).

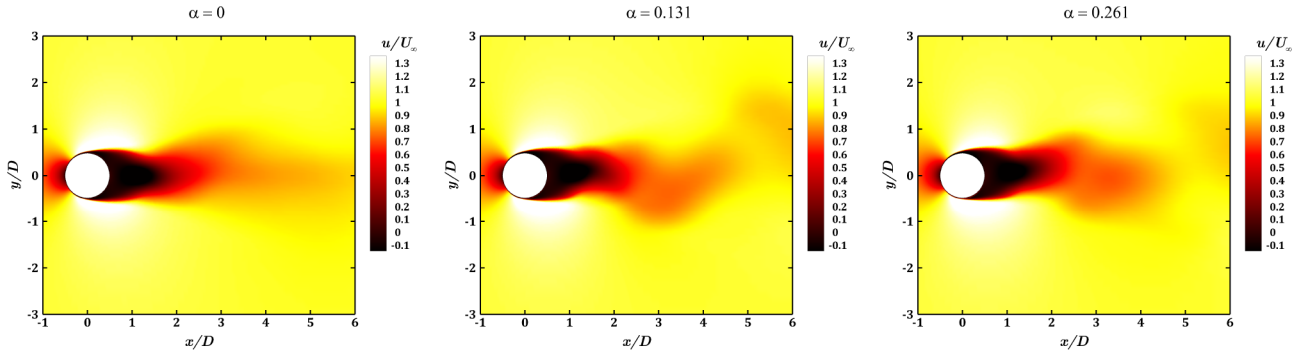

(a) (b) (c)

Fig. 19. Mean stream-wise velocity contour for various dimensionless ratio (Re = 9400).

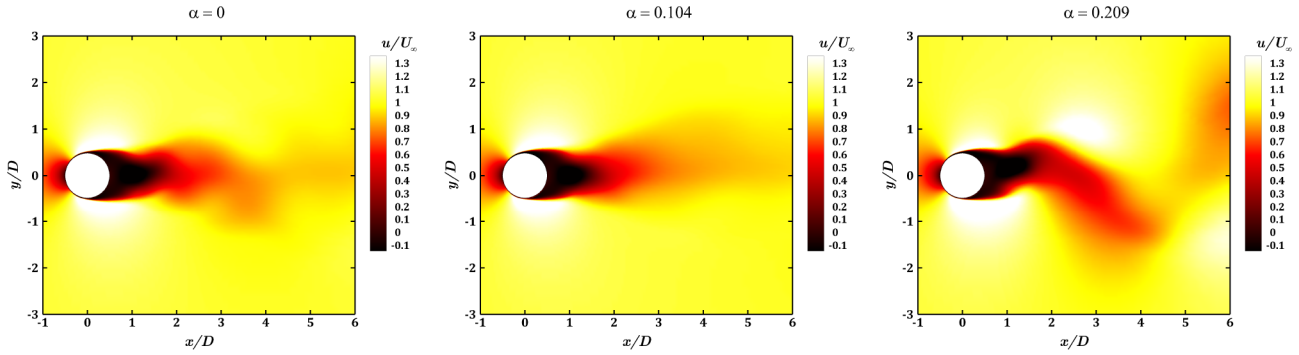

(a) (b) (c)

Fig. 20. Mean stream-wise velocity contour for various dimensionless ratio (Re = 11800).

occurs at higher angels due to the presence of adverse flow and co-flow on the upper and lower surfaces, respectively. Finally, comparing the three diagrams shows that the wake upward inclination as well as the wake length decrease as the Reynolds number increases. Furthermore, it is observed that increasing the spin ratio would lead to a decrease in the width of the wake area behind the cylinder.

4.3 Calculation of drag coefficient using wake-survey method

One of the methods for calculating the drag force is "*momentum difference*" method, which is used in several studies. Van Dam [48] used the continuity equations and linear momentum for the control volume capturing the body and considered Reynolds stresses in determination of the drag force coefficient. Goldstein [49] determined the static pressure in the wake region by measuring the air flow velocity in the wake region as well as the 3-D turbulence. As the distance from the model increases, the intensity of the air turbulence decreases and the turbulences can be assumed homogeneous. In such condition, using a 1-D HW probe, the drag force can be measured (see the reference [29] for more details).

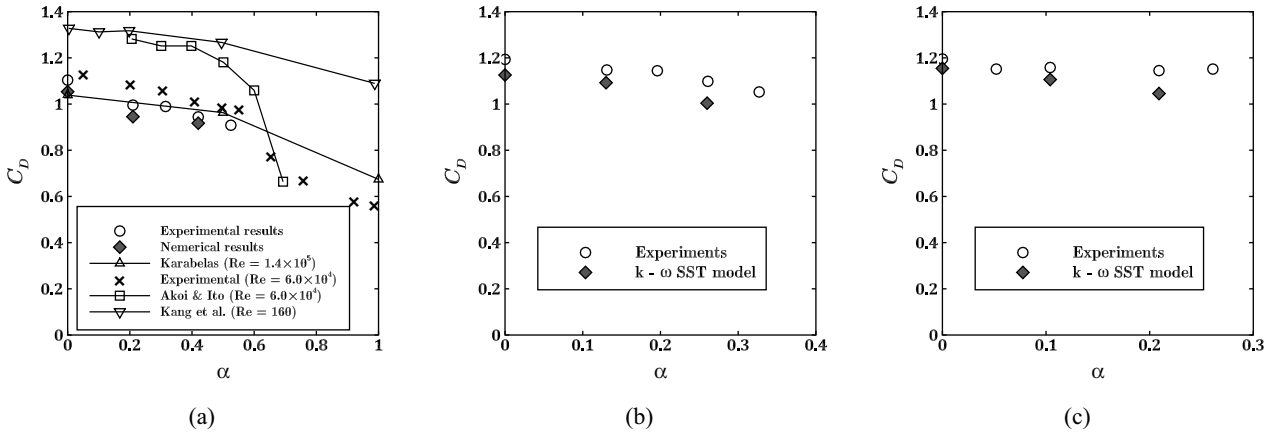

Fig. 21. Variations of the drag coefficient for various dimensionless ratio; (a) Re = 5900, (b) Re = 9400, and (c) Re = 11800.

Drag force coefficient can be calculated by following equation:

$$C_D = 2\int_{-\infty}^{+\infty} \frac{U}{U_\infty}\left(1-\frac{U}{U_\infty}\right)\mathrm{d}\left(\frac{y}{l}\right) + \int_{-\infty}^{+\infty} \frac{\overline{v'^2}+\overline{w'^2}-\overline{u'^2}}{U_\infty^2}\cdot\mathrm{d}\left(\frac{y}{l}\right) \tag{11}$$

in which, v' and w' are the transverse fluctuation of the airflow velocity. eq. (11) is known as the "*modified Van Dam equation*".

Assuming the homogeneous turbulence intensity ($u' = v' = w'$), eq. (11) can be simplified and expressed by eq. (12)

$$C_D = 2\int_{-\infty}^{+\infty} \frac{U}{U_\infty}\left(1-\frac{U}{U_\infty}\right)\mathrm{d}\left(\frac{y}{l}\right) + \int_{-\infty}^{+\infty} \frac{\overline{u'^2}}{U_\infty^2}\cdot\mathrm{d}\left(\frac{y}{l}\right) \tag{12}$$

The first term is the difference of the time-averaged momentum flow field and the second term shows the distribution of turbulence fluctuations. In all of the conducted experiments, 10–20% of the total drag coefficient was due to the second term.

In order to measure the drag coefficient in highly turbulent and inhomogeneous flows by momentum difference method, measurements should be conducted at appropriate intervals in the downstream. In closer distances, in addition to air flow velocity, Reynolds stresses should also be measured for calculating the drag force. Therefore, determination of the Reynolds stress is of particular importance. If the air flow turbulence in the downstream region is homogeneous, the drag coefficient can be measured by the use of a 1-D hot-wire anemometry probe, which only measures the turbulence intensity along the flow direction. In the present study, the drag coefficient is obtained from the velocity profiles and fluctuations of wake at $x/D = 18$. The rotational effects have largely influenced the pressures imposed by the fluid.

Figure 21(a)–(c) represent the diagrams of drag coefficient *versus* spin ratio at different Reynolds numbers obtained from the present work and the results of Kang [14] for the Reynolds number of 160, Aoki and Ito [50] for the Reynolds number of 6.0×10^4, the experimental results presented in reference [51] at Reynolds number 6.0×10^4 and the results of Karabelas [52] for the Reynolds number of 1.4×10^5. While the flows in those studies were considered to be laminar and with high Reynolds number, this comparison shows that the current results have an appropriate trend. The results of time-averaged drag coefficient are completely consistent with the experimental results of this study and other researches. The maximum difference between numerical and experimental results is about 10%.

According to fig. 21(a), drag coefficient decreases by increasing the spin ratio, due to the upward displacement of the front stagnation point in the high pressure region. In the case of stationary cylinder, the high pressure region is at the middle of the left semi-cylinder. Therefore, the net pressure force, which is the main component of pressure drag, is exerted on the surface along the centerline in the direction of the flow. When the stagnation point moves upward, the exertion point of the net pressure force also moves upward, so the force is no longer in the direction of the flow, and consequently, the component of the net pressure force along the flow decreases, which results in a subsequent decrease in the pressure drag.

Figure 21(b), (c) shows the variation of drag coefficient with Reynolds number at different spin ratios. It can be seen that drag coefficient is generally increased by increasing the Reynolds number; however the slope decreases by increasing the spin ratio. Usually, Reynolds number increases by increasing the free stream velocity. At a constant spin ratio, increase of the free stream velocity should be accompanied with the increase of angular velocity, so that the spin ratio remains constant. As a result, both rotational speed and free stream velocity are increased. The effect of

the former is to increase the upward dislocation of stagnation point, but the latter has an opposite effect. Therefore, for smaller spin ratios, the effect of velocity increase is much higher than the effect of rotational speed and hence, the curves are decreased with larger slopes. For the higher spin ratios, the condition is opposite and rotational speed becomes more effective and hence, the stagnation point is displaced a little, and the curves have smaller slopes. In addition to the above discussion, through the careful observation of the velocity contour diagrams, it can be figured out that the wake area behind the cylinder becomes narrower by the increase of Reynolds number in a constant spin ratio. It means that the overall pressure on the right half of the cylinder increases and hence the drag force decreases.

5 Conclusion

In the present paper, experimental and numerical investigations of the flow around a circular cylinder at Reynolds numbers between 5900 and 11800 and spin ratios between 0 and 0.525 have been carried out. In experimental tests, an open-circuit wind tunnel was used and data acquisitions were conducted in three longitudinal sections behind the cylinder. In addition, hot-wire anemometry was used to measure the streamwise mean velocity and velocity fluctuation profiles. Moreover, the wake-survey method was employed for calculation of the drag coefficient and for simulating the turbulent flow, the k-ω SST model was utilized. This article addressed two major issues: first, the variation of flow wake at lower rotation rates of cylinder, and second, the significance of the Reynolds number for the flow wake of the cylinder. The obtained results are:

- Streamwise mean velocity and fluctuating velocity profiles are dependent on the Reynolds number and spin ratio.
- By increasing the distance from cylinder, the streamwise mean velocity and turbulence intensity profiles become more uniform and are inclined downward. Also, peaks in the turbulence intensity profile occur at positions with high-velocity gradients in the mean velocity profile. It was also found that with an increase in the Reynolds number, the mean velocity and turbulence intensity increase within the wake region.
- It was shown that at spin ratios between 0 and 0.525, the shear layers interfere and vortex shedding takes place. Furthermore, rotation causes the deflection of the wake in the tangential velocity direction and therefore, smaller shear layers would be observed.
- Increase in the spin ratio leads to an increase in velocity within the vortex and to a decrease in velocity outside the wake region. In addition, when the symmetry is broken during the rotation, the length of the shear layers on both sides of the cylinder would be different.
- The present study showed that the variation in spin ratio may significantly influence the velocity fluctuations in the downstream of the recirculation region. For $\mathrm{Re} = 5900$ and at $\alpha \geq 0.42$, it was observed that velocity fluctuations are higher in the downstream of the recirculation region which will be decreased by enhancement of x/D. For $\alpha < 0.42$, however, we have an ascending-descending trend. For the case of $\mathrm{Re} = 9400$ and $\alpha \geq 0.192$, we saw that velocity fluctuations are higher in the downstream of the recirculation region while we had an increasing-decreasing trend for $\alpha < 0.192$. We found that a further increase of the Reynolds number to 11800 will decline the velocity fluctuations in the wake edges.
- Negative skewness peaks were employed to determine the wake boundaries. Based on our results, the increase of the spin ratio along with the enhancement of the Reynolds number may be associated with a decline in the length of the mean recirculation region and the presence of shorter wakes behind the body.
- The results indicate that by increasing the Reynolds number, the wake region formed behind the cylinder becomes smaller. Moreover, the structure of the flow is changed in the stagnation and separation point.
- Furthermore, flow separation is delayed in the downstream of the moving wall, whereas the separation point in the upstream moving wall moves along the wind.
- It was observed that for $\mathrm{Re} = 5900$, increase of α will enhance the Strouhal number whereas the Strouhal number remained unchanged by further increase of α. This observation again highlights the significance of the flow field properties at the end of the mean recirculation region and its immediate downstream, which is the origin of the vortex shedding.
- Any variation in the flow field is associated by variation of the force coefficients. It was observed that by increasing the spin ratio, the drag coefficient decreases. Namely, at $\mathrm{Re} = 5900$ and $\alpha = 0.42$, the drag coefficient is $C_D = 1.22$, while at $\alpha = 0$ the drag coefficient is reduced about 14%. The obtained numerical results are in good agreement with experimental data.
- In summary, the investigation of the Reynolds number showed a strong dependence of the flow around a cylinder on the rotation rate and its weak dependence to Reynolds number. Finally, the Reynolds number and the rotation rate are the two significant parameters with substantial influence on the flow wake of a rotating cylinder.

References

1. P.W. Bearman, Annu. Rev. Fluid Mech. **16**, 195 (1984).
2. A. Radi, M. Thompson, A. Rao, K. Hourigan, J. Sheridan, J. Fluid Mech. **734**, 567 (2013).
3. M. Gad-el Hak, D.M. Bushnell, J. Fluids Eng. **113**, 5 (1991).
4. A. Martin-Alcantara, E. Sanmiguel-Rojas, R. Fernandez-Feria, J. Fluids Struct. **54**, 868 (2015).
5. O.M. Griffin, M. Hall, J. Fluids Eng. **113**, 526 (1991).
6. A. Rao, A. Radi, J.S. Leontini, M.C. Thompson, J. Sheridan, K. Hourigan, J. Fluid Mech. **769**, R2 (2015).
7. J. Meena, S. Mittal *et al.*, J. Fluid Mech. **766**, 28 (2015).
8. P. Tokumaru, P. Dimotakis, J. Fluid Mech. **224**, 77 (1991).
9. V. Modi, F. Mokhtarian, M. Fernando, T. Yokomizo, J. Aircr. **28**, 104 (1991).
10. L. Prandtl, Naturwissenschaften **13**, 93 (1925).
11. D. Ingham, T. Tang, J. Comput. Phys. **87**, 91 (1990).
12. H. Badr, S. Dennis, P. Young, Comput. Fluids **17**, 579 (1989).
13. Y.M. Chen, Y.R. Ou, A.J. Pearlstein, J. Fluid Mech. **253**, 449 (1993).
14. S. Kang, Phys. Fluids **18**, 047106 (2006).
15. H. Chen, V. Patel, AIAA J. **26**, 641 (1988).
16. S. Mittal, B. Kumar, J. Fluid Mech. **476**, 303 (2003).
17. H. Badr, M. Coutanceau, S. Dennis, C. Menard, J. Fluid Mech. **220**, 459 (1990).
18. Y. Chew, M. Cheng, S. Luo, J. Fluid Mech. **299**, 35 (1995).
19. M.J. Ezadi Yazdi, A. Bak Khoshnevis, J. Turbul. **19**, 529 (2018).
20. A. Bak Khoshnevis, M.J. Ezadi Yazdi, E. Gholiepour Asrami, J. Mech. Eng. **45**, 39 (2015).
21. W. Chen, C.-K. Rheem, J. Mar. Sci. Technol. **24**, 111 (2019).
22. O. Lehmkuhl, I. Rodríguez, R. Borrell, J. Chiva, A. Oliva, Phys. Fluids **26**, 125110 (2014).
23. W. Cheng, D. Pullin, R. Samtaney, W. Zhang, W. Gao, J. Fluid Mech. **820**, 121 (2017).
24. S. Karabelas, B. Koumroglou, C. Argyropoulos, N. Markatos, Appl. Math. Modell. **36**, 379 (2012).
25. W. Cheng, D. Pullin, R. Samtaney, J. Fluid Mech. **855**, 371 (2018).
26. D. Aljure, I. Rodriguez, O. Lehmkuhl, C.D. Pérez-Segarra, A. Oliva, Int. J. Heat Fluid Flow **55**, 76 (2015).
27. G. Smaism, O. Fatla, A. Valera Medina, A. Rageb, N. Syred, Int. J. Energy Environ. **7**, 23 (2016).
28. M.J. Ezadi Yazdi, A. Bak Khoshnevis, Eur. Phys. J. Plus **133**, 533 (2018).
29. M. Ardekani, F. Farhani, A. Nourmohammadi, Flow Meas. Instrum. **50**, 237 (2016).
30. F.R. Menter, AIAA J. **32**, 1598 (1994).
31. H. Schlichting, K. Gersten, *Boundary-Layer Theory* (Springer, 2016).
32. S. Sarkar, S. Sarkar, J. Fluids Struct. **26**, 19 (2010).
33. P. Bearman, J. Fluid Mech. **21**, 241 (1965).
34. O.M. Griffin, S.E. Ramberg, J. Fluid Mech. **66**, 553 (1974).
35. A. Mariotti, G. Buresti, M. Salvetti, Eur. J. Mech. B/Fluids **74**, 351 (2018).
36. I. Wygnanski, H.E. Fiedler, J. Fluid Mech. **41**, 327 (1970).
37. G. Fabris, Phys. Fluids **26**, 1437 (1983).
38. A. Mariotti, G. Buresti, Exp. Fluids **54**, 1612 (2013).
39. A. Mariotti, G. Buresti, G. Gaggini, M. Salvetti, J. Fluid Mech. **832**, 514 (2017).
40. A. Mariotti, J. Wind Eng. Ind. Aerodyn. **176**, 21 (2018).
41. R. Antonia, P.Å. Krogstad, Fluid Dyn. Res. **28**, 139 (2001).
42. G. Buresti, P. Petagna, A. Talamelli, Exp. Therm. Fluid Sci. **17**, 18 (1998).
43. F. Diaz, J. Gavaldà, J. Kawall, J. Keffer, F. Giralt, Phys. Fluids **26**, 3454 (1983).
44. J. Jaminet, C.C.W. Va, AIAA J. **7**, 1817 (1969).
45. S. Kumar, C. Cantu, B. Gonzalez, J. Fluids Eng. **133**, 041201 (2011).
46. S. Kang, H. Choi, S. Lee, Phys. Fluids **11**, 3312 (1999).
47. J. Calvert, J. Fluid Mech. **27**, 273 (1967).
48. C.P. Van Dam, Prog. Aerosp. Sci. **35**, 751 (1999).
49. S. Goldstein, Proc. R. Soc. Lond. A **155**, 570 (1936).
50. K. Aoki, T. Ito, Proc. School Eng. Tokai Univ. **26**, 29 (2001).
51. A. Elmiligui, K. Abdol-Hamid, S. Massey, S. Pao, in *22nd Applied Aerodynamics Conference and Exhibit* (AIAA, 2004) p. 4959.
52. S. Karabelas, Int. J. Heat Fluid Flow **31**, 518 (2010).